Journal of Electroanalytical Chemistry xxx (2011) xxx–xxx

Contents lists available at ScienceDirect

Journal of Electroanalytical Chemistry

journal homepage: www.elsevier.com/locate/jelechem

Numerical and experimental studies of Electrochemical Deposition quasi-stable growth

Esteban E. Mocskos [a], Graciela González [a,b,1], Fernando V. Molina [a,b], Guillermo Marshall [a,*,1]

[a] Laboratorio de Sistemas Complejos, Departamento de Computación, Facultad de Ciencias Exactas y Naturales, Universidad de Buenos Aires, Pabellón 1, C1428EGA Buenos Aires, Argentina
[b] INQUIMAE, Facultad de Ciencias Exactas y Naturales, Universidad de Buenos Aires, 1428 Buenos Aires, Argentina

ARTICLE INFO

Article history:
Received 15 August 2010
Received in revised form 11 December 2010
Accepted 15 December 2010
Available online xxxx

Keywords:
Electrochemical Deposition
Numerical simulation
Growth pattern formation

ABSTRACT

Electrochemical Deposition (ECD) in thin cells in a vertical position relative to gravity (cathode above anode) yields a growth pattern formation with a uniform front. However, detailed analysis of front evolution reveals a complex competition between neighboring branches leading to a locally fluctuating growth. We study these fluctuations through experiments and theory. Experiments reveal that the uniform dendrite front is due to an acceleration and deceleration of the leading branches, the latter resulting from the building of a stable stratified flow at their tips. Theory predicts local electrohydrodynamic fluctuations near the dendrite tips amid a global stable stratified flow. Dendrite tips are surrounded by arches joining neighboring tips, separating depleted and constant concentration solution zones; the arches shape is the result of electro and gravitoconvective driven vortex rings. The simulated growth of a single tip exhibits the formation of a mushroom-like shape which is consistent with experimental observations.

1. Introduction

In thin-layer cell Electrochemical Deposition (ECD) experiments [1–26] dendrite growth is accompanied by a complex physicochemical hydrodynamic ion transport process. Ion transport is mainly governed by diffusion, migration and convection, and convection is mostly driven by coulombic forces due to local electric charges and by buoyancy forces due to concentration gradients that lead to density gradients.

Convection certainly increases ECD complexity and it is natural to try to reduce its influence [27,28,12,13,29,30,22] ECD in a cell in a vertical position relative to gravity and with the cathode above the anode is often used as an example of a convection reduced ion transport regime. This problem was analyzed in Huth et al. [12]; these authors found that the invasion of the cell by the gravity induced rolls can be avoided while electroconvection remains. In this configuration, a stratified flow emerges and no gravitoconvection is present as long as no growth appears. According to these authors, when growth appears horizontal concentration gradients drive convection near the growing tips of the dendrites, a competition emerges in which convective motion feeds branches lagging behind until they catch up with the leader; convection inhibits competition between branches, leading to a uniform front rather than a hierarchy of branch sizes as seen in horizontal cells [12]. This is illustrated in Fig. 1, reproduced from Dengra [24], showing two schlieren images of a dendrite deposit growing from the cathode towards the anode (dark pixels) and the corresponding concentration fronts (bright pixels). Fig. 1a with a rather uniform front corresponds to a cell in the vertical position (top cathode), while Fig. 1b with a hierarchy of branch sizes corresponds to a cell in the horizontal position (left cathode).

Since the only change in the experiments of Fig. 1, is the direction of gravity relative to the electric force (which remains invariant relative to cell position), no doubt gravity is the main cause of the difference growth behavior between both experiments. However, gravity acts in a subtle interplay with electric forces and electrochemical reactions revealing complex pathways that need to be unveiled for understanding the balancing mechanisms giving rise to smooth dendrite fronts. We carry out this analysis by means of extensive experimental measurements and the introduction of a theoretical 3D model with a new aggregation model.

The plan of the paper is the following. Section 2 shows the experimental setup, the phenomenological model and experimental results are introduced in Sections 3. Section 4 presents the theoretical model and numerical simulations. Finally, Section 5 draws some general conclusions.

* Corresponding author. Tel.: +54 11 4576 3390/96 709.
E-mail addresses: emocskos@dc.uba.ar (E.E. Mocskos), graciela@qi.fcen.uba.ar (G. González), fmolina@qi.fcen.uba.ar (F.V. Molina), marshalg@retina.ar (G. Marshall).
[1] Consejo Nacional de Investigaciones Científicas y Técnicas.

1572-6657/$ - see front matter © 2010 Elsevier B.V. All rights reserved.
doi:10.1016/j.jelechem.2010.12.019

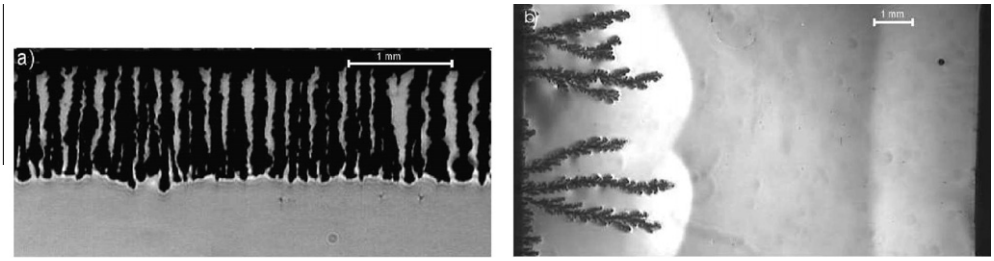

(a) Vertical cell with cathode above anode (the plane of the cell is parallel to gravity)

(b) cell in the horizontal position (the plane of the growth is normal to gravity)

Fig. 1. Schlieren images of ECD where copper sulfate solution concentration is 0.5 mol/l, the cell width is 0.2 mm and the applied constant voltage is 15 V.

2. Experimental

The cell consists of a thin layer of unsupported electrolyte confined between two parallel glass plates. The electrolyte solution was 0.05–0.3 mol/l $CuSO_4$. To increase viscosity, for some experiments, a solution with a glycerol addition of 30% in weight was employed. Copper plate electrodes were placed at the two ends of the cell with a separation $L = 10$ mm; their thickness (0.127–0.2 mm) defined the thickness, d, of the cell. The cell width was $w = 70$ mm. The schlieren method was used to observe electrolyte concentration gradients. The optical setup is similar to that described in Marshall et al. [31].

For fluid tracking, latex spheres 0.9 μm in diameter were added to the electrolyte as flow visualization particles. To observe them, a Navitar long working distance microscope was used. Video images were digitized and saved to disk at up to 10 frames/s with spatial resolution of up to 3.5 μm/pixel (a public domain software package [32] was used for image capturing and processing).

3. Results

Fig. 2 presents schlieren snapshots of ECD in a vertically oriented cell showing the evolution of the deposit front and the cathodic and anodic concentration fronts. The deposit front looks rather smooth in the average, dendrite tips surrounded by tenuous concentration arches joining neighboring tips. The shape of the arches is the result of electroconvection and local gravitoconvection.

We next analyze the nature of this quasi-stable growth. Fig. 3 presents an enlarged image of a small section of a dendrite front showing the fluctuating growth evolution of a branch and its neighbors. Once a branch is detached from its neighbors (Fig. 3a left branch), its tip enlarges adopting the shape of an inverted mushroom; the process progresses until the leading branch levels with the lagging branches, as can be seen in Fig. 3d. Fig. 3e shows the birth of newer leading branches. The sequence repeats itself, however no hierarchical branching develops and the front remains globally uniform with local fluctuations.

We will show that the fluctuating growth is produced by the acceleration and deceleration of the leading branch, the latter being produced as a result of the presence of a stratified flow in its front.

To understand the nature of this quasi equilibrium growth we analyze the interplay of electric and gravity forces mediated by this complex electrohydrodynamic process. For this, we need to introduce the macroscopic phenomenological model describing ECD in a cell in a vertical position with the cathode above the anode. Naturally, the model has many features in common with ECD in a cell in an horizontal position. When the circuit is closed, current starts flowing through the cell and ion concentration boundary layers develop near each electrode. At the anode the concentration is increased above its initial level due to the transport of anions towards, and the dissolution of metal ions from the anode.

At the cathode, the ion concentration is decreased as metal ions are reduced and deposited out and anions drift away. These concentration variations lead to density variations, and therefore to concentration fronts at the electrodes. In this configuration the high density fluid is below the low density fluid, hence a stable stratified flow emerges in which gravitoconvection is suppressed. Stratification remains stable as long as there is no growth of dendrites.

During this initial period, ion transport is mainly diffusive and migratory and cation depletion at the cathode is expected to be uniform. Consequently, in a very narrow region near the cathode a local uniform charge develops, giving rise to local electric forces initially pointing towards the cathode. After a few seconds, an instability develops, triggering the growth of a deposit at the cathode.

The deposit develops as a three-dimensional (3D) array of thin porous metallic filaments. Electric forces concentrate at the tips; each porous filament allows fluid to penetrate its tip and to be ejected from the sides, forming a vortex ring driven by the electric force. But, as soon as dendrites appears, stratification breaks down because the fluid concentration surrounding a downward growing dendrite tip diminishes, creating an horizontal concentration gradient and thus, locally gravitoconvection. Clearly, the presence of dendrites generates a vortex tube driven by gravity which adds to the vortex ring driven by local electric charges. In spite of this local breaking of symmetry, at nude eye, the deposit front looks smooth rather than with a hierarchy of branch sizes.

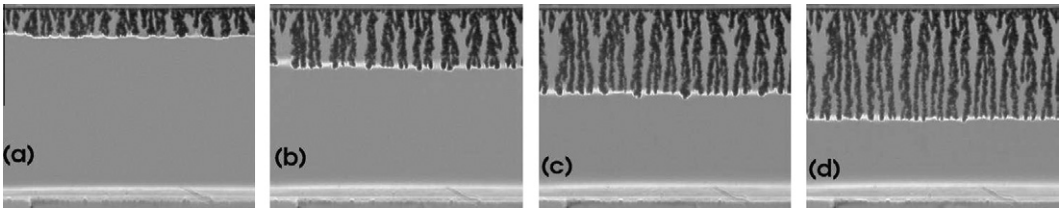

Fig. 2. Schlieren images of ECD in a vertical oriented cell at (a) 80 s, (b) 160 s, (c) 240 s and (d) 320 s. Copper sulfate solution concentration is 0.1 mol/l, the cell dimensions are $70 \times 10 \times 0.2$ mm^3 and the applied constant current is 7.5 mA.

Please cite this article in press as: E.E. Mocskos et al., J. Electroanal. Chem. (2011), doi:10.1016/j.jelechem.2010.12.019

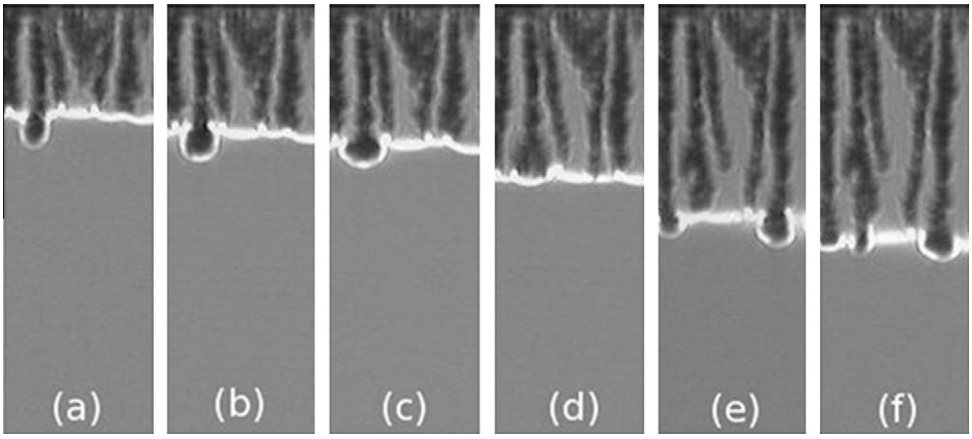

Fig. 3. Enlarged schlieren images of ECD in a vertically oriented cell at (a) 160 s, (b) 185 s, (c) 200 s, (d) 250 s, (e) 300 s and (f) 325 s showing the growth fluctuation. Copper sulfate solution concentration is 0.1 mol/l, the cell dimensions are $70 \times 10 \times 0.2$ mm^3 and the applied constant current is 7.5 mA.

Fig. 4 shows three sequences of experiments of ECD in vertical cell with the cathode above the anode: A, B, and C. Each sequence with increasing value of the concentration and electric currents, shows the time evolution of the dendrite growth. In all the experiments we observe a relatively uniform dendrite front and when a leading branch succeeds in detaching from its neighbors, it enlarges and slows down until it levels with the rest, that conserve a constant speed. This is proven in Fig. 5 that presents the front tracking of the three numbered branches from experiment A from Fig. 4. Fig. 5 shows that the leading branch first accelerates and then decelerates allowing neighboring branches to level with the leader.

Clearly, neighboring branches maintain a constant speed, it is the leading branch that fluctuates in its growth velocity. This is valid for all the concentrations analyzed.

Thus, to complete the phenomenological model under galvanostatic conditions, the following explanation is advanced. Due to an instability produced by the appearance of local electric charges at a certain branch, the local electric field at the tip of that branch increases, accelerating and detaching the branch from its neighbors.

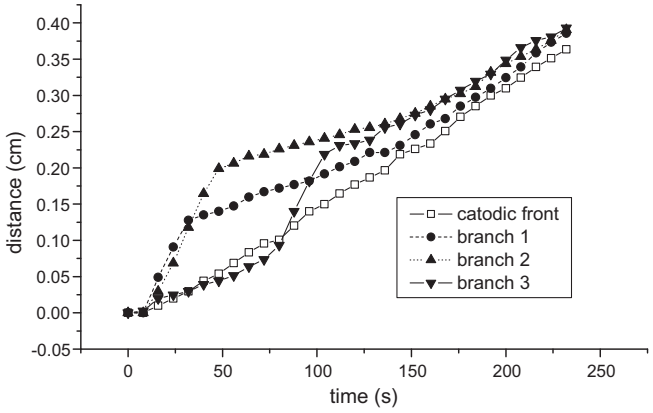

Fig. 5. Front tracking of the three selected branches of experiment A from Fig. 4.

This happens when the local electric field in front of a lagging branch increases due to a sudden decrease in the concentration

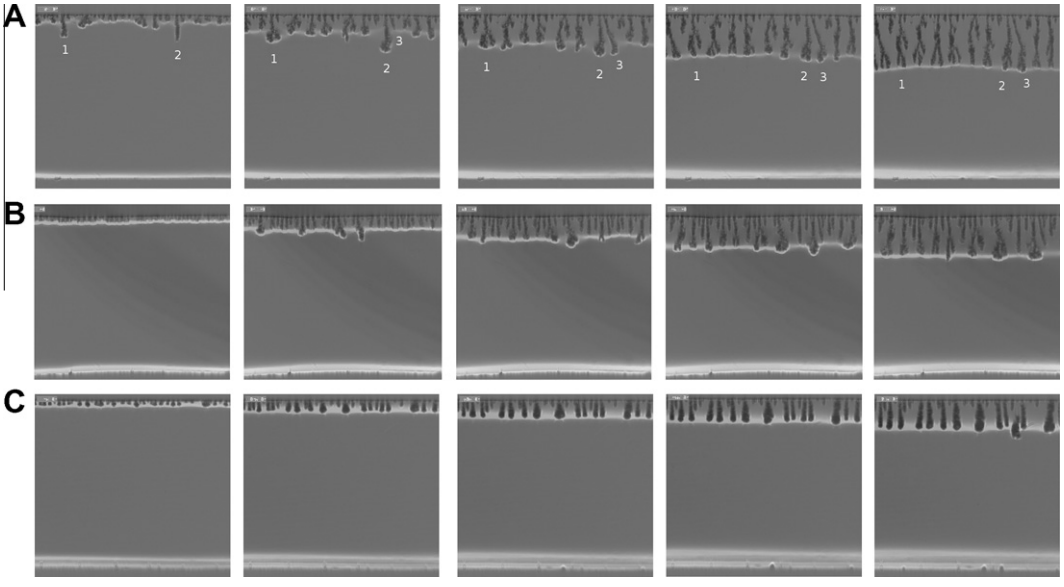

Fig. 4. Schlieren images of ECD in a vertically oriented cell at 80 s, 160 s, 240 s, 320 s, and 400 s (from left to right): (A) 0.05 mol/l copper sulphate with 30% glycerol added, $I = 2$ mA, initial voltage: 15.6 V; (B) 0.1 mol/l copper sulphate with 30% glycerol added, $I = 2$ mA, initial voltage: 6.2 V; (C) 0.3 mol/l copper sulphate with 30% glycerol added, $I = 5$ mA, initial voltage: 9.4 V (copper electrodes separation: 1 cm, thickness: 0.127 cm).

Please cite this article in press as: E.E. Mocskos et al., J. Electroanal. Chem. (2011), doi:10.1016/j.jelechem.2010.12.019

level and shots the branch to the front. During the leading branch detachment and acceleration, lateral concentration gradients surrounding the leading branch develop yielding a buoyancy force; this force is proportional to the length of the leading branch detachment from its neighbors. Though electric forces and gravity forces have the same direction and opposite sign, electric forces and buoyancy forces have the same sign, thus electrically driven vortex rings and gravity driven vortex tubes rotate in the same direction adding their strengths. Every further detachment of the leading branch due to the electric force give rise to a larger buoyancy force that increase the vortex tube relative to the vortex ring. The net result of this competition is an upwards motion of the combined vortex centroid. Growth fluctuates according to the time scales imposed by electric and gravity forces, in which the former is the fastest one. There is another phenomenon modifying the growth pattern. During branch detachment from its neighbors, the leading branch encounters a region of higher concentration (stratified flow) surrounding its front and sides which has two effects: a decreasing of the local electric field and an increase of the aggregation at its sides giving rise to a mushroom-like shape (electric field lines converge radially to the leading branch tip); in turn, this mushroom effect further decreases the local electric field at the tip due to local charge spread. These combined effects decelerate the leading branch until it levels with the lagging branches that kept a constant speed.

In general, as shown in Fig. 4 branch fluctuation decreases with higher concentrations. A possible cause of this is that the electric field decreases with higher concentrations, and thus front velocity that is proportional to the electric field. The net effect is more damped fluctuations of the local flow (gravito and electroconvective) and dendrite growth, thus a more uniform deposit front.

To show that the fluctuating mechanism is robust regardless of the initial front configuration, this is to say, that the front remains uniform once the effect of the initial perturbation dies away, we present a comparison of two identical experiments in Figs. 6 and 7, except that in the former there is a single spike in an otherwise flat cathode. In both experiments schlieren snapshots of dendrite growth are presented. Focusing on the zone where the spike is located (whether with or without spike), the leading branch velocity (in Fig. 6) remains smaller than the velocity of its neighbors until the leading branch levels with them. Again, the main cause of this behavior is that the leader encounters a higher concentration solution and thus a weaker local electric field. Fig. 7 shows that without the presence of the spike, the front remains uniform and similar to that of Fig. 6 when sufficiently time has elapsed and spike perturbation faded.

In both cases the front advances at the same speed once the leader branch levels with its neighbors. The front velocity on the spike zone is the same in both experiments and smaller than in the rest of the deposit front. In the spike zone the front adopts an inverted mushroom shape.

To study in detail the behavior in a zone near a single spike, such as the one in Fig. 6, or a small detachment (fluctuation) of a branch from its neighbors as the one in Fig. 3, we present in Fig. 8 an ECD experiment in a vertical cell in which the single spike or the leading branch is mimicked by a small spike in an otherwise flat cathode. Fig. 8 shows nine frames in lexicographic ordering of the evolution of the growth and the hydrodynamics surrounding the spike. Here convection is visualized using micron sized tracer particles; 100 snapshots (a 10 s interval) are superimposed in each frame to show motion. The resulting motion is the effect of the superposition of two pairs of counter-rotating vortices due to local buoyancy and electric forces, and its coupling with the growth process. As clearly seen the flow pattern determines the lateral growth and in turn, the latter influences vortex formation.

4. Theoretical analysis and numerical simulations

Ion transport in thin-layer ECD can be described with a mathematical model based on first principles [33–36], including the Nernst–Planck equations for ion transport, the Poisson equation for the electric potential, and the Navier–Stokes equations for the fluid flow. The 3D dimensionless system of equations can be written as

$$\frac{\partial C_i}{\partial t} = -\nabla \cdot \mathbf{j}_i \tag{1}$$

$$\mathbf{j}_i = -M_i C_i \nabla\phi - \frac{1}{Pe_i}\nabla C_i + C_i \mathbf{v} \tag{2}$$

$$\nabla^2\phi = Po\sum_i z_i C_i \tag{3}$$

$$\frac{\partial \boldsymbol{\zeta}}{\partial t} + \nabla \times (\boldsymbol{\zeta} \times \mathbf{v}) = \frac{1}{Re}\nabla^2\boldsymbol{\zeta} + \sum_i \left[G_e z_i (\nabla\phi \times \nabla C_i) - G_{g_i} \nabla \times \left(C_i \frac{\mathbf{g}}{g} \right) \right] \tag{4}$$

$$\boldsymbol{\zeta} = -\bigtriangledown^2 \Psi \tag{5}$$

$$\mathbf{v} = \bigtriangledown \times \Psi \tag{6}$$

Here C_i and $\mathbf{j}_i$ are the dimensionless concentration and flux of an ionic species i (for a ternary electrolyte such as $ZnSO_4/H_2SO_4$, i = C, A and H, standing for zinc, sulphate and hydrogen ions); $\mathbf{v}$, ϕ, $\boldsymbol{\zeta}$ and $\boldsymbol{\Psi}$ are the dimensionless fluid velocity, electrostatic potential, vorticity vector and velocity potential vector, respectively; $\mathbf{g}/g$ is a unit vector pointing in the direction of gravity. The quantities $M_i = \mu_i\Phi_0/x_0u_0$, $Pe_i = x_0u_0/D_i$, $Po = x_0^2C_0e/\epsilon\Phi_0$, $Re = x_0u_0/\nu$, $G_e = eC_0\Phi_0/\rho_0u_0^2$ and $G_{g_i} = x_0C_0g\alpha_i/u_0^2$, stand for the dimensionless numbers Migration, Peclet, Electric Poisson, Reynolds, Electric Grashof and Gravity Grashof numbers, respectively. The quantities z_i, μ_i, and D_i are, respectively, the number of charges per ion, mobility and diffusion constants of an ionic species i; μ_i and z_i are signed quantities, being positive for cations and negative for anions; g is the dimensional gravitational acceleration; e is the electronic charge, ϵ is the permittivity of the medium and ν is the kinematic viscosity. x_0, u_0, ϕ_0, C_0, and ρ_0 are reference values of the length, velocity, electrostatic potential, concentration, and fluid density, respectively. For system closure, a Boussinesq-like approximation has been used for the fluid density: $\rho = \rho_o(1 + \Sigma_i\alpha_i\Delta C_i)$, where $\alpha_i = \frac{1}{\rho_o}\frac{\partial\rho}{\partial C_i}$.

Systems (1)–(6), with appropriate initial and boundary conditions, is valid in a space–time domain defined by $\mathbf{G} = [\Omega(t)x(0,t)]$, where Ω is a three-dimensional region with boundary $\Gamma(t)$; this boundary moves with speed proportional to the norm of the flux $\mathbf{j}_i$.

The boundary conditions for the vorticity vector $\boldsymbol{\zeta}$ and the velocity vector potential $\boldsymbol{\Psi}$ are derived from the velocity boundary conditions (walls are assumed impermeable). This implies that $\boldsymbol{\Psi}$ is normal to the boundary and that the normal derivative of its normal component is zero. For example, at $x = 0$, $\partial\psi_1/\partial x = \psi_2 = \psi_3 = 0$. This, together with no-slip condition at the walls, yields conditions for $\boldsymbol{\zeta}$, for example, at $x = 0$, $\zeta_1 = 0$, $\zeta_2 = -\partial^2\psi_2/\partial x^2$, $\zeta_3 = -\partial^2\psi_3/\partial x^2$. Here, we assume $\boldsymbol{\Psi} = \psi_1\boldsymbol{i} + \psi_2\boldsymbol{j} + \psi_3\boldsymbol{k}$ and $\boldsymbol{\zeta} = \zeta_1\boldsymbol{i} + \zeta_2\boldsymbol{j} + \zeta_3\boldsymbol{k}$, respectively, where $\boldsymbol{i}$, $\boldsymbol{j}$, $\boldsymbol{k}$ are the unit vectors in the x, y and z directions. Details of all the boundary conditions used can be found in Mallinson and de Vahl Davis [37,38].

The computational model solves the previous 3D system of equations, for each time step, in a fixed or variable domain, in a 3D uniform lattice, using finite difference and deterministic relaxation techniques. Its solution is obtained via the system of difference equations:

$$\mathbf{W}_k^{n+1} = \sum_j \mathbf{a}_j \mathbf{W}_j^n \tag{7}$$

where j represents the nearest-neighbor site of the site k; the summation ranges over all nearest-neighbor sites; $\mathbf{W}_k$ is a vector-valued

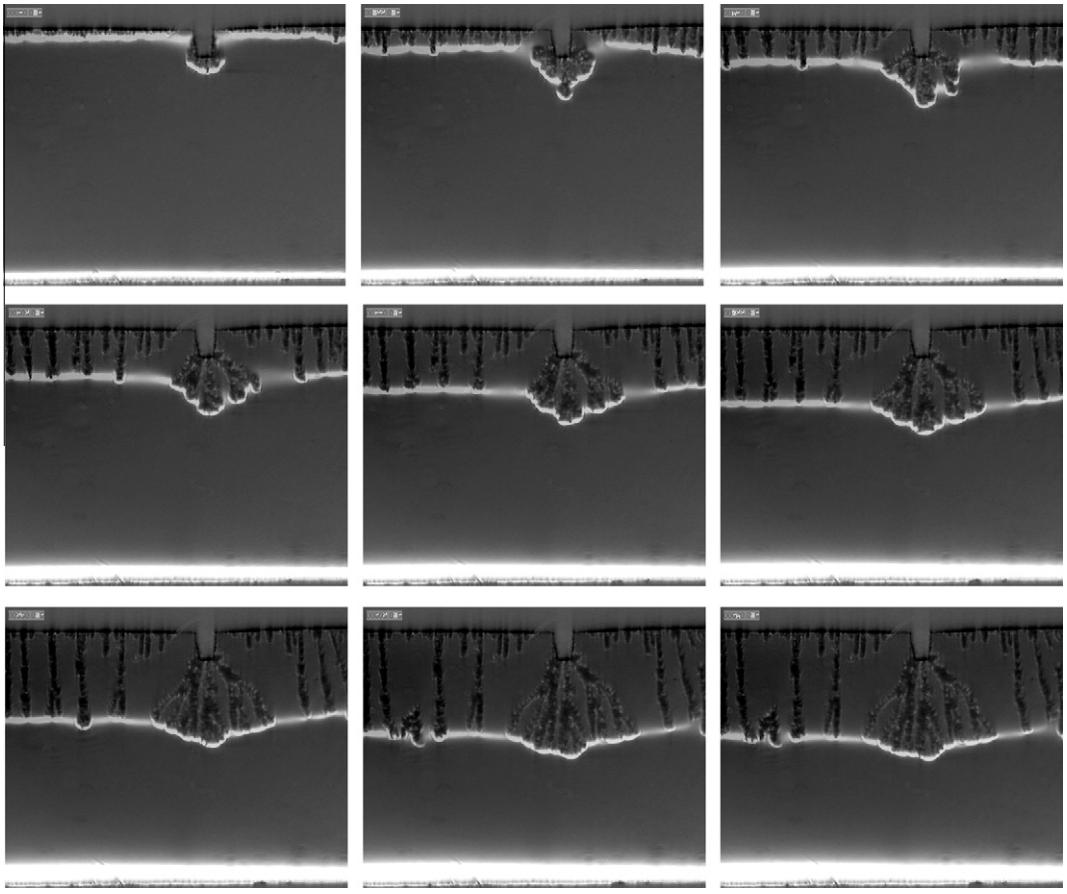

Fig. 6. Schlieren snapshots of dendrite growth with a single artificial spike in an otherwise flat cathode.

function whose components are the concentrations C_i, the electrostatic potential ϕ, the vorticity vector ζ and velocity potential vector $\mathbf{\Psi}$; and $\mathbf{a}_j$ is a diagonal matrix whose elements contain the nonlinear coefficients of the discretized equations. The resulting solution $\mathbf{W}_k^{n+1}$ is then used to advance the interface with a Dielectrical Break-down Model (DBM) [39]. The interface is moved at random, proportional to the flux of cations, i.e.,

$$p_k = \frac{|\mathbf{j}_{c_k}|}{\sum_i |\mathbf{j}_{c_i}|} \tag{8}$$

where k is a nearest neighbor site to the interface, p_k is the probability of selecting the nearest-neighbor site k to advance the interface, the summation is over all nearest neighbor sites i to the interface, and $\mathbf{j}_{c_k}$ is the flux of cations flowing from the neighbor site k into the aggregation.

The computational model is written in the `C` language and implemented on an Intel Xeon 64 dual processor dual core. Graphics are done with the plotting package `OpenDx` [40].

To show the existence of the hydrodynamic structures underlying growth in cells in horizontal and in vertical position relative to gravity and to reveal their differences we present the following numerical results.

Fig. 9 shows simulations for a cell in a horizontal position with three spikes of different length to mimic hierarchical dendrite growth. Fig. 10 shows simulations for a cell in a vertical position with three spikes of equal length to mimic global uniform dendrite growth. In all the simulations we assumed a binary electrolyte. A typical cell is represented by a cubic grid of $240 \times 60 \times 160$ nodes. The dimensionless numbers used are: $M_a = 0.625$, $M_c = 0.42$, $Pe_a = 2.4$, $Pe_c = 3.6$, $Po = 1.9 \times 10^2$, $Re = 2.5 \times 10^{-3}$, $Ge = 1 \times 10^4$, $Gg_a = 2.0 \times 10^4$ and $Gg_c = 1.33 \times 10^4$. These numbers correspond to the experiment presented in Fig. 1 except for the real Poisson and Electric Grashof numbers (in the order of 1×10^8 and 1×10^{12} cm^{-3}, respectively, see González et al. [21]), which cannot be handled, because they produce unstable numerical solutions.

Fig. 9 shows snapshots at 30 s, 40 s, 50 s and 60 s, of the cell in a horizontal position. Fig. 9a shows the initial formation of the cathodic and anodic vortex tubes evidenced by particle trajectories released at different locations in the cell and anion concentration shells, superimposed with cathodic and anodic cation iso-concentration shells. There is a coalescence among individual rolls of adjacent filament tips resulting in a more uniform cathodic front. This front is defined by dendrites and their vortex rings pushing the front forward. Trajectories of particles released near the dendrite tips reveal the entangled nature of flow: near the dendrite tips the fluid is entrained by vortex rings whose basin of attraction is the dendrite tip. However, some particles manage to escape and are entrained by the vortex roll, finally orbiting with a helicoidal motion. Particle trajectories also show vortex interaction among themselves in the presence of dendrites, in an analogy with the physical experiments from Fig. 1b. Fig. 9b shows a cross-section of the velocity profile at mid cell, superimposed also with cathodic and anodic cation iso-concentration shells. Trajectories reveal the evolution of cathodic and anodic convective and concentration fronts. In particular, they unveil how density currents generate gravity driven rolls consisting in horizontal cylinders squeezed at their extremes due to lateral wall effects. While the anodic roll remains undisturbed, the cathodic roll is wrapped around the electrode spikes. The snapshot shows the precise moment in which

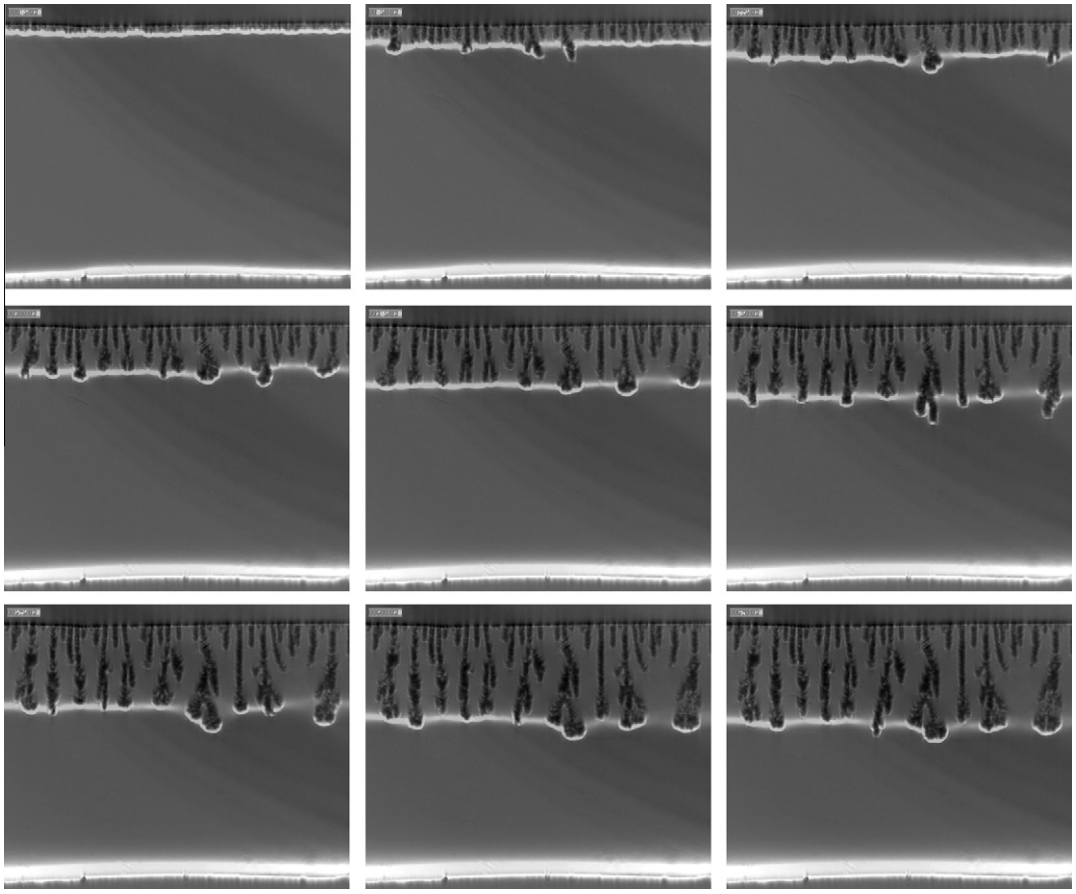

Fig. 7. Schlieren snapshots of dendrite growth on a flat cathode.

the cathodic and anodic rolls collide and merging starts. The evolution of concentration shells follows closely the evolution of rolls since rolls are slaved to shells.

Fig. 9c shows an isosurface of the modulus of the velocity potential vector and two contours (y and z constant) at the moment in which both fronts collided and merged into one single roll occupying the whole cell. Clearly, in a horizontal cell vortexes expand and invade the whole cell.

Fig. 9d shows the electric field lines in a plane passing through a mid horizontal cross-section of the cell. The spheroids with the shape of a drop surrounding the spike tips represent an iso-surface of the modulus of the electric field. Electric field lines are almost undisturbed and parallel except near the spikes tips to which they converge.

Fig. 10a–d shows snapshots of the cell in a vertical position, cathode above anode. Fig. 10a shows anion concentration isosurfaces in the cell superimposed with particle trajectories released in a zone near the three spikes. The figure reveals the presence of a global stratified flow except in the zone near the spikes in which a local convection regime exists. This convection is the result of vortex tube and ring superposition. Vortex tube and vortex ring remain attached to the spike tips. Fig. 10b shows concentration shells and velocity field in a cross-section at mid cell. Concentration shells remain wrapped to the spike tips. Away from them there is a stratified flow. At the bottom there is no vortex tube because of complete flow stratification and thus, absence of gravity convection. There are clearly seen the differences between Fig. 9a and b (horizontal case) and Fig. 10a and b (vertical case). Fig. 10c shows concentration shells and vortex tube and rings superimposed wrapped to the spike tips. Comparing Fig. 10c with Fig. 9c, we observe that in the former the cathodic vortex tube splits in three due to the separation among spikes. Have the spikes been closer, the vortex would have coalesced.

Fig. 10d shows electric field lines and an iso-surface of the modulus of the electric field near the spike tips. Comparing with Fig. 9d, reveals that both are quite similar, thus showing that gravity is the main cause of the hydrodynamic differences observed between horizontal and vertical cells.

To summarize the theoretical predictions of the different behavior of ECD in cells in a vertical position (cathode above anode) relative to gravity and cells in a horizontal position: a horizontal cell always leads to a constrained unstable flow regime; a vertical stable cell comprises two flows regimes: (a) in the absence of dendrites, a globally stable stratified flow regime in which there is no convection and the ECD process is migration and diffusion controlled; (b) in the presence of dendrites, a quasi-stable flow regime in a zone near the dendrites, in which there is local convection and the ECD process is migration, diffusion and convection controlled; outside that region, the flow is stably stratified. In the horizontal case, ECD always leads to a constrained unstable flow regime, however, the orientation of the cell walls relative to gravity, impedes the development of a full unstable flow; moreover, the cathodic and anodic vortex rolls invade the whole cell, colliding and merging into each other. In a vertical cell , vortex rolls only exist near the cathode or the deposit and remain attached to them. There is no vortex roll at the anode due to stratification. The electric field distribution is almost the same in the horizontal and vertical cells. Since the only change in both cases is the direction of gravity relative to the electric field, clearly gravity is the main cause of the differences in the growth and flow regimes.

Please cite this article in press as: E.E. Mocskos et al., J. Electroanal. Chem. (2011), doi:10.1016/j.jelechem.2010.12.019

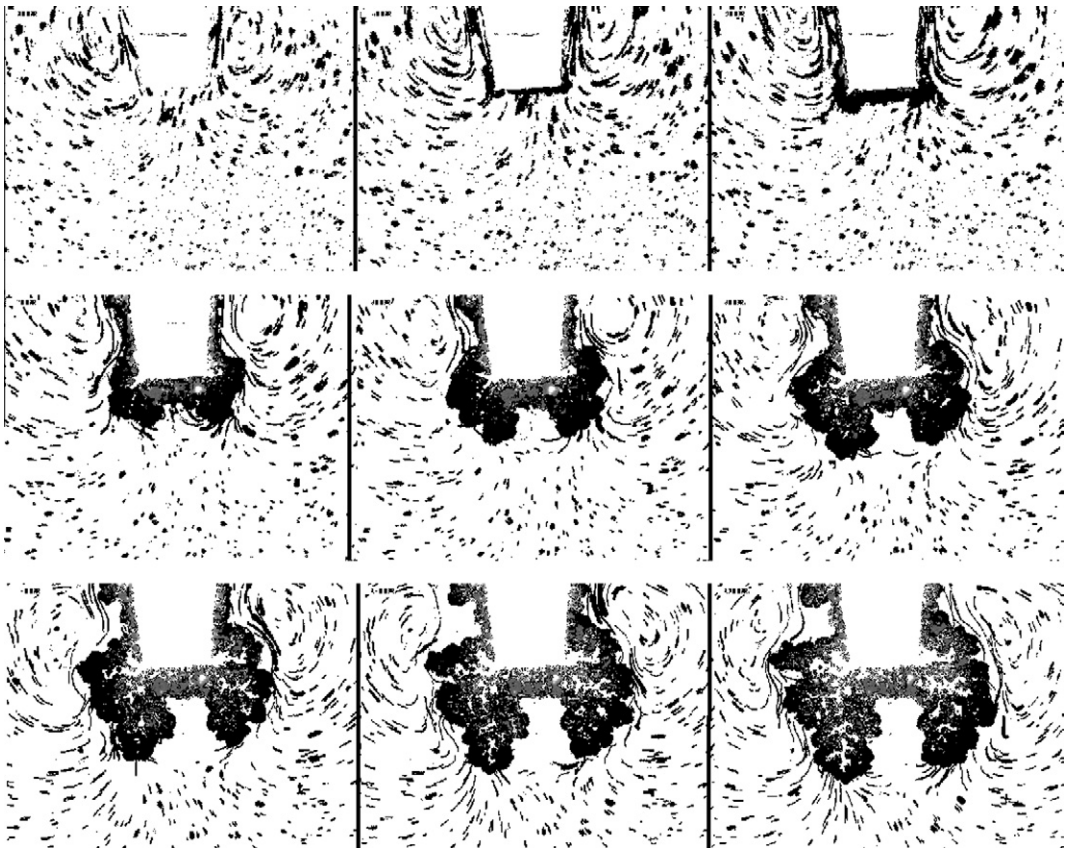

Fig. 8. Visualization of 1 μm sized particle trajectories near the cathode spike (amplified). To show the motion of tracer particles, 100 digital images were superimposed in each frame, comprising nine frames in lexicographic ordering in the 0–90 s time interval. Copper sulfate solution concentration is 0.1 mol/l with 30% glycerol in weight, the cell dimensions are $70 \times 10 \times 0.127$ mm^3, the applied constant current is 2 mA and the spike dimensions are $1 \times 0.5 \times 0.127$ mm^3.

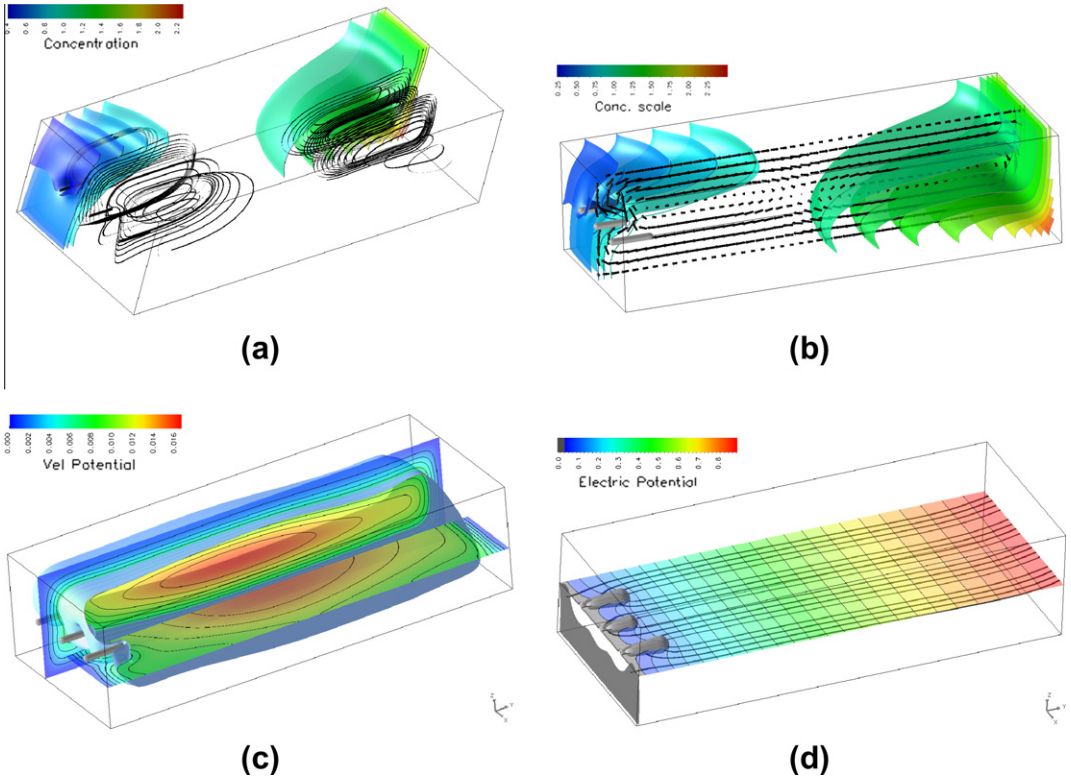

Fig. 9. Snapshots of the horizontal cell simulation with three spikes at different times. (a) particle trajectories and anion concentration isosurfaces, (b) cross-section of the velocity profile at mid cell, superimposed also with cathodic and anodic cation iso-concentration shells, (c) isosurface of the modulus of the velocity potential vector and two contours (y and z constant), and (d) electric field lines in a plane passing through a mid horizontal cross-section of the cell.

Please cite this article in press as: E.E. Mocskos et al., J. Electroanal. Chem. (2011), doi:10.1016/j.jelechem.2010.12.019

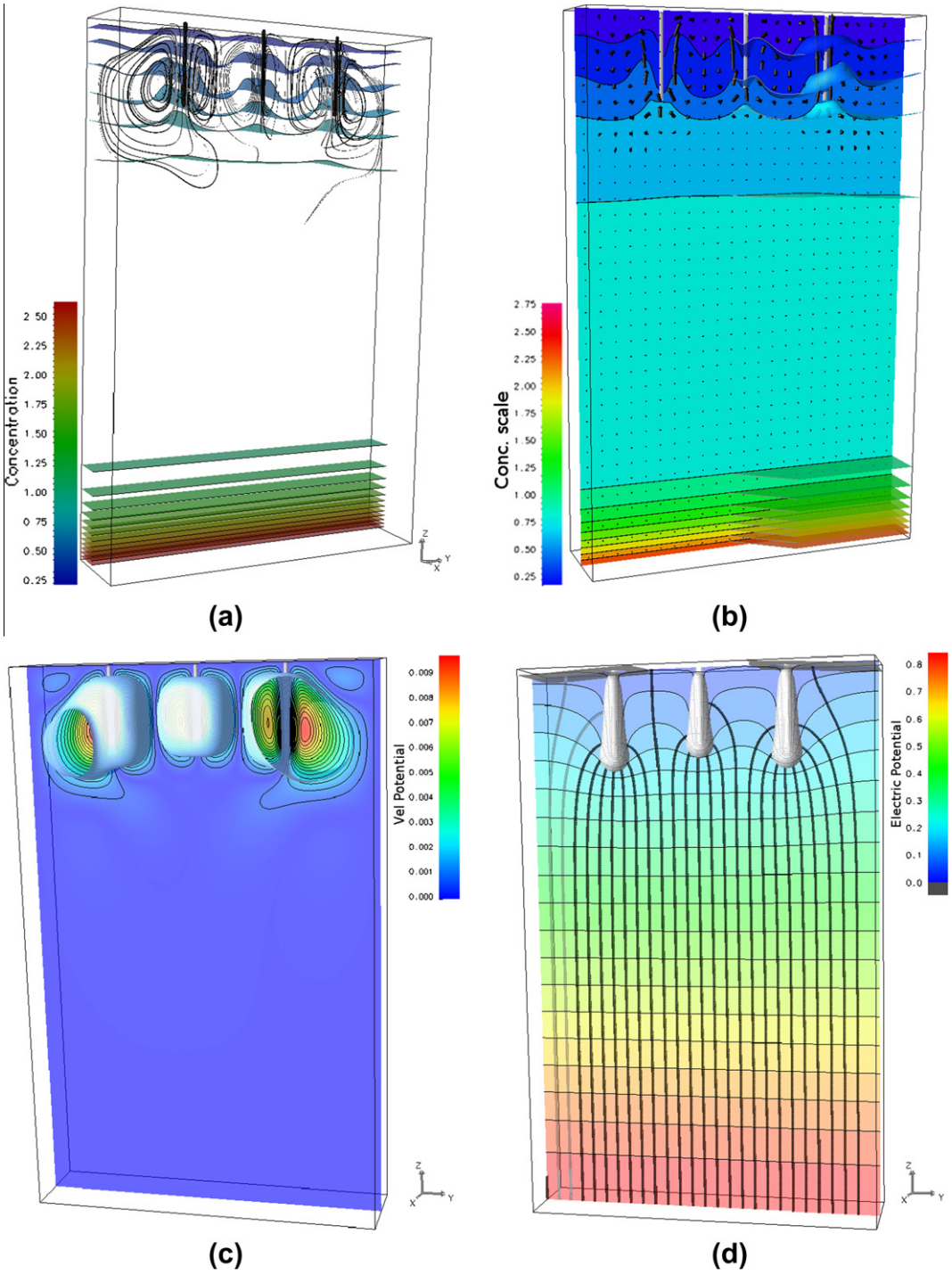

Fig. 10. Snapshots of the vertical cell simulation (cathode above anode) with three spikes. (a) Vortex tube and ring revealed by particle trajectories released near the three spikes superimposed with anion isoconcentration surfaces, (b) anion isoconcentration surfaces and velocity field, (c) isosurfaces of the modulus of the vector potential near spikes, and (d) electric field lines and isosurface of the modulus of the electric field near the spikes.

To study the electrohydrodynamic pattern of ECD in a vertical cell with a single spike, such as that shown in Fig. 6 or in Fig. 8 we used a cubic grid of $30 \times 120 \times 200$ nodes. Fig. 11 shows numerical results of ECD in a vertical cell with a single spike (enlarged) in an otherwise flat electrode. Fig. 11a displays numerical schlieren superimposed to concentration contours. Near the spike, the white zone indicates the vortex tube and ring wrapped to the spike. Fig. 11b displays a geometric form with the approximate shape of a spherical drop (gray area turned slightly transparent) representing an isosurface of the modulus of the electric field, and a cross-section (at spike level) of the electric field lines. Fig. 11c shows concentration shells and particles, released near the spike, evidencing the vortex tube and ring superimposed. Fig. 11d displays concentration shells and the velocity field. It is observed that on most of the cell motion is suppressed and no vortex tube exists at the anode. These simulations have some resemblance with the experiments of Fig. 6 or its analogy, Fig. 8.

To study in detail the relative strength of electrically driven vortex rings and gravity driven vortex tubes in an ECD experiment in a vertical cell with one single spike Fig. 12 shows numerical results

Please cite this article in press as: E.E. Mocskos et al., J. Electroanal. Chem. (2011), doi:10.1016/j.jelechem.2010.12.019

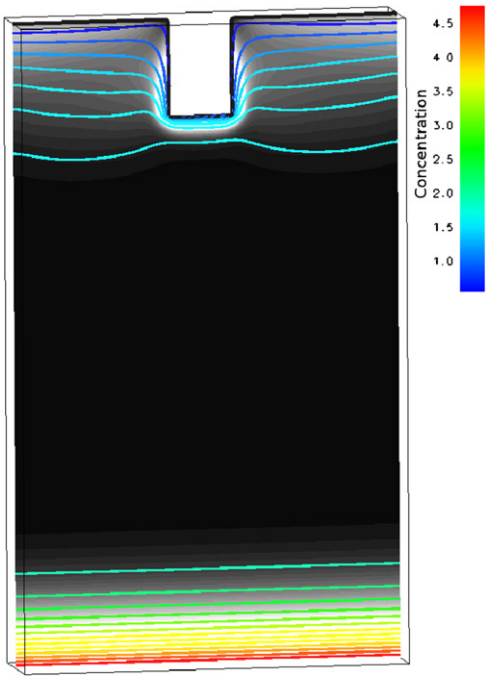

(a) Numerical schlieren image with concentration contour lines superimposed.

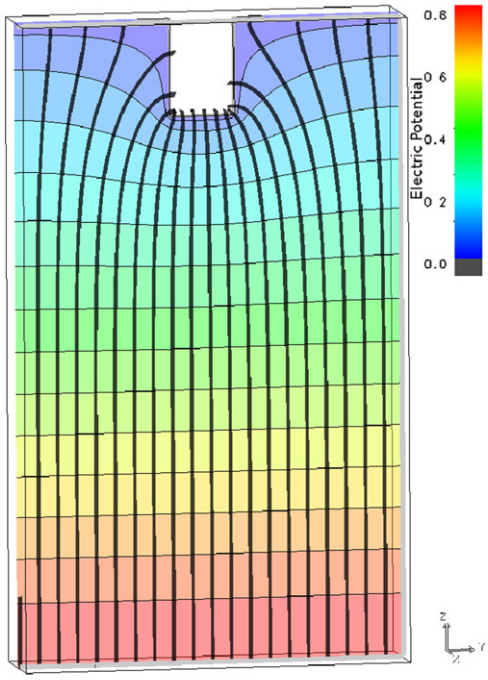

(b) Electric field lines superimposed with electrostatic potential contour lines.

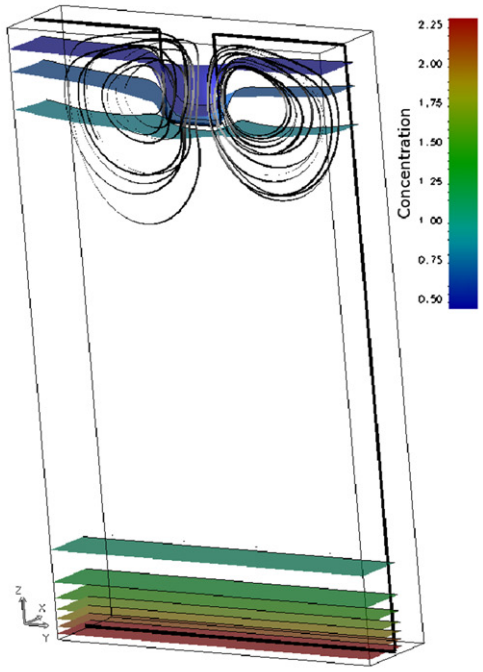

(c) Particle trajectories superimposed with anion concentration contour lines.

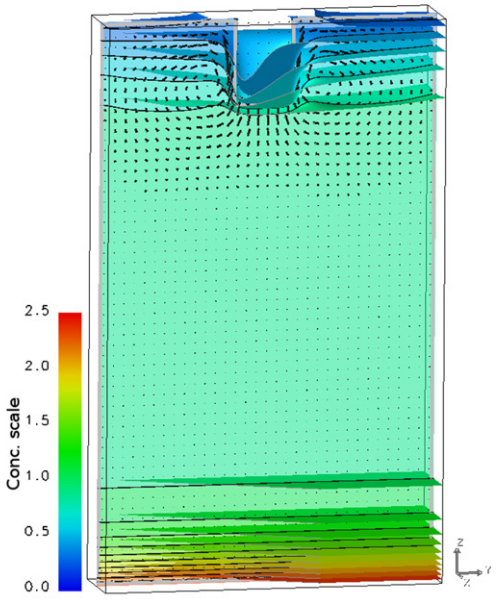

(d) Velocity field superimposed with anion concentration contour lines.

Fig. 11. Flow pattern simulation near a spike in a vertical cell (cathode above anode), reproduced from Mocskos and Marshall [26].

for a single artificial spike in an otherwise flat cathode. Fig. 12a presents results for the case in which gravity forces prevail over electric forces (Gravity Grashof number is larger than Electric Grashof number) while Fig. 12b presents the opposite case. Fig. 12 shows a snapshot at 3.91 s of an iso-surface of the modulus of the velocity vector potential around the spike tip superimposed with a contour of that surface in a cross-section at mid cell. Comparing both plots in Fig. 12 reveals that the shape of the isosurface of the modulus of the velocity vector potential is more elongated in the z direction and slender in the left plot, while it is shorter in the z direction and wider in the right plot, due to the prevailing conditions of tube and ring, respectively. The net effect of buoyancy is to move up the centroid of the modulus of the velocity vector potential. Fig. 13a and b shows the corresponding plots of the concentration isosurfaces at different levels superimposed with various trajectories of tracking particles released near the spike. Again, it

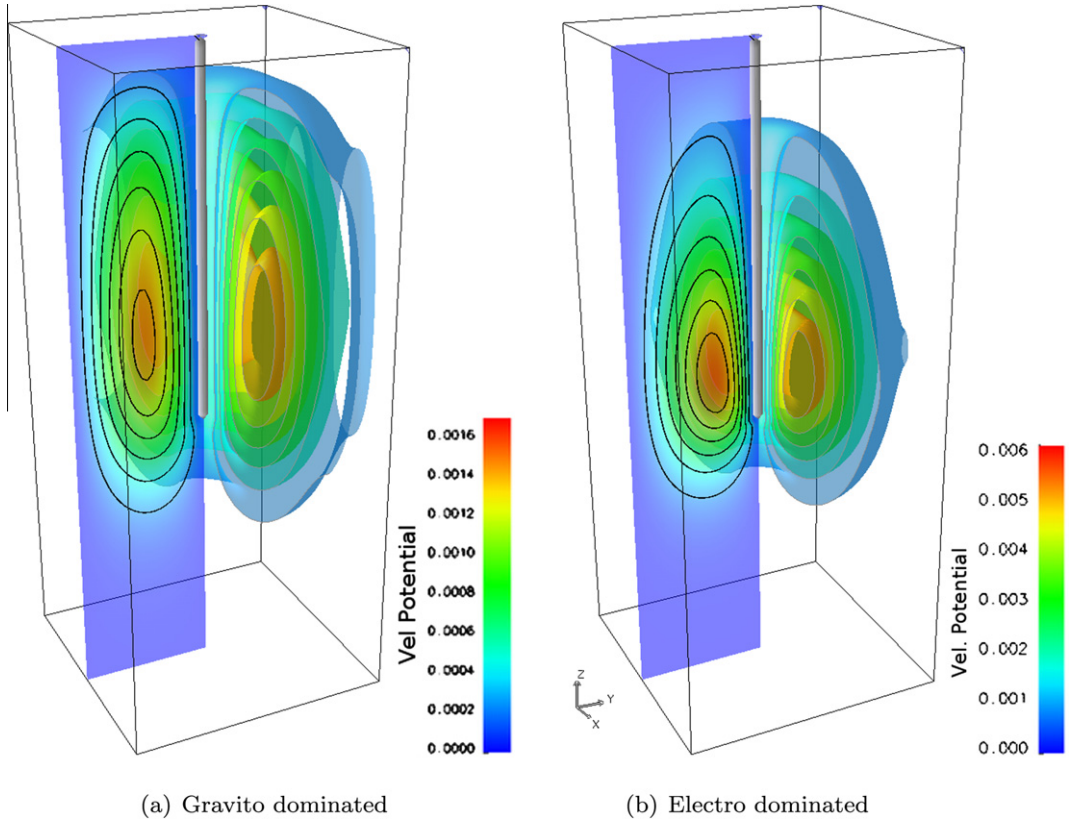

Fig. 12. Comparison between gravity dominated (a) vs. electrodominated (b) regimes. Left and right plots show isosurfaces of the modulus of the velocity vector potential and contour lines in a plane passing trough the cell center. The color scale was selected to emphasize different intensities around the growth in both cases, notice that there is factor of almost three between them. (For interpretation of the references to color in this figure legend, the reader is referred to the web version of this article.)

is noted here the impact of gravity in the spreading of the concentration and particle trajectories.

Fig. 14a presents a numerical schlieren snapshot of ECD in a vertical cell with three spikes in an otherwise flat cathode showing schlieren and concentration contour lines. Again, Fig. 14a reveals the dendrite tips wrapped by cathodic concentration arches joining neighboring tips and separating depleted and concentrated solution zones. Such behavior is consistent with the experimental snapshot of Fig. 14b.

Fig. 15 shows the genesis of the growth of a single branch tip (a square spike or finger protruding from the cathode) as it grows, its tip enlarging and splitting in the form of two inverted mushrooms, and its interaction with the underlying vortex dynamics. These simulations intend to mimic the growth of the ECD experiment presented in Fig. 6 or its analogy, Fig. 8, consisting in a ECD in a vertical cell with the growth of small spike in an otherwise flat cathode. Numerical images show the evolution of the velocity field superimposed with an anion isoconcentration surface, in a longitudinal cross-section at the cell center. The isoconcentration surface is taken close to the finger growth, thus indicating the growth as a mushroom-like shape. The hydrodynamic pattern near the growth results from a composition of the vortex tube driving by local gravitoconvection and the vortex ring driven by electroconvection. Away from the cathode, there is a stratified flow with a complete absence of convection as in the experiments.

5. Conclusions

We reported experimental measurements of ECD with a cell in the vertical position and the cathode above the anode, and we introduced a 3D theoretical macroscopic model with a stochastic aggregation model for dendrite growth and numerical simulations. Experimental measurements demonstrate that the quasi equilibrium growth giving rise to a uniform dendrite front is due to an acceleration and deceleration of the leading branches, the latter resulting from the building of a stable stratified flow at their tips. Basically, once a branch detaches from its neighbors and accelerates due to an increase in the local electric field becoming a leader branch, it encounters a region of higher concentration surrounding its front and sides which has the effect of increasing the aggregation at the sides and giving rise to a mushroom-like shape. This shape increases the local charge spread, decreases the local electric field and thus decelerates the leader branch, until it levels with lagging branches that kept a constant speed.

Theory and simulations predict that when no growth of dendrites is present, the flow is globally stable. When dendrites are present the fluid concentration near a downward growing tip is lowered thus generating a vortex tube (driven by gravitoconvection) superposed to a vortex ring (driven by electroconvection) wrapping the dendrite tip (much as in the case of the horizontal cell in which the dendrite tip is surrounded by gravito- and electroconvective vortices, respectively). Local flow at the tips is the result of vortex tube and vortex ring superposition: both have the same sign, that is, at the tip's left and right sides, both vortices are clockwise and counter clockwise, respectively. Electroconvective vortices allow fluid to penetrate at the tip and be ejected from its sides. The region close to the anode is not affected by the growth and remains without convection. This yields a quasi-stable flow regime, i.e. the presence of local electrohydrodynamic fluctuations near the dendrite tips amid a global stable stratified flow. The

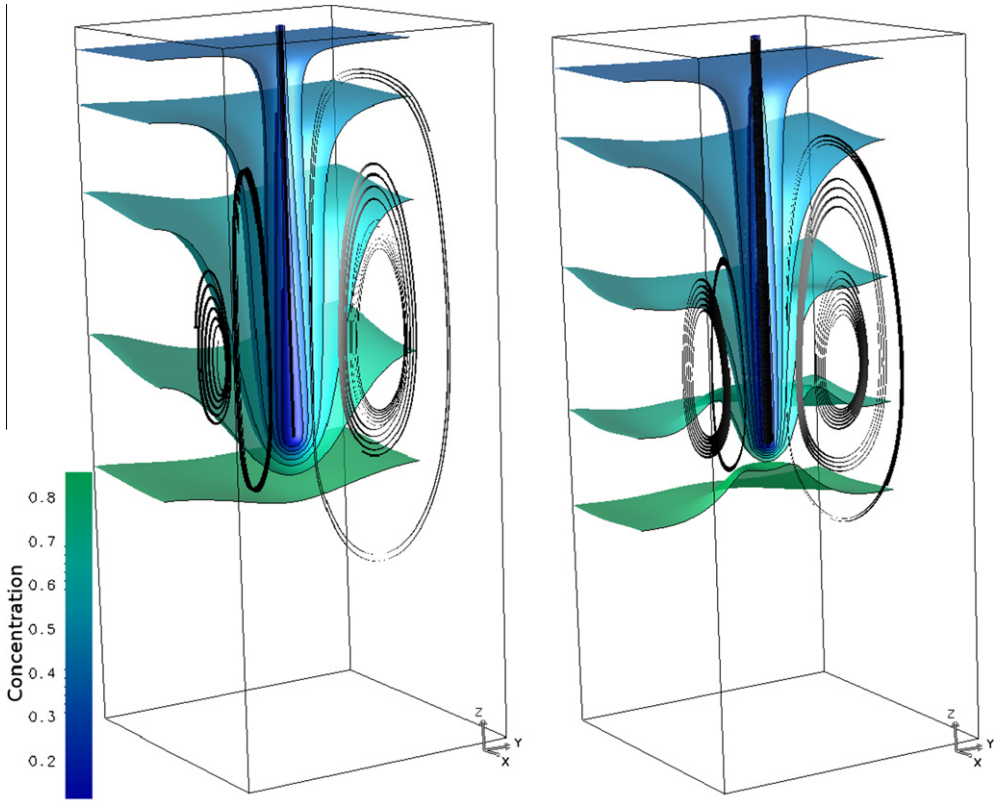

(a) Gravito dominated (b) Electro dominated

Fig. 13. Comparison between gravity dominated (a) vs. electrodominated (b) regimes. Left and right plots show isoconcentration surfaces (using the same color scale) and particle trajectories released near the spike. (For interpretation of the references to color in this figure legend, the reader is referred to the web version of this article.)

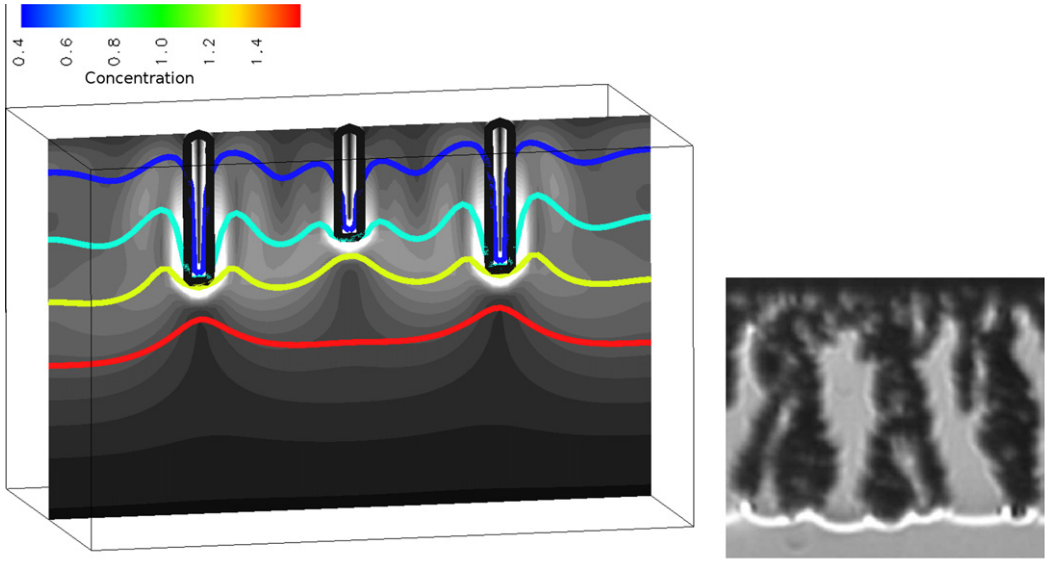

(a) Simulated schlieren image and concentration contour lines in a virtual three spike growth deposit

(b) Zoom from figure 2 at 100s.

Fig. 14. Simulated schlieren and concentration contour lines in the enlarged zone near the cathode with a three spike growth showing the formation of the arches separating high and low concentration values. (b) Shows the experimental formation of these structures.

dendrite tips are surrounded by cathodic concentration arches joining neighboring tips separating depleted and concentration solution zones. The shape of these arches is the result of the merging of electro and gravito convective driven vortex rings. The simulated growth of a single tip exhibits the formation of a mushroom-like shape. Such behavior is observed in experiments.

Please cite this article in press as: E.E. Mocskos et al., J. Electroanal. Chem. (2011), doi:10.1016/j.jelechem.2010.12.019

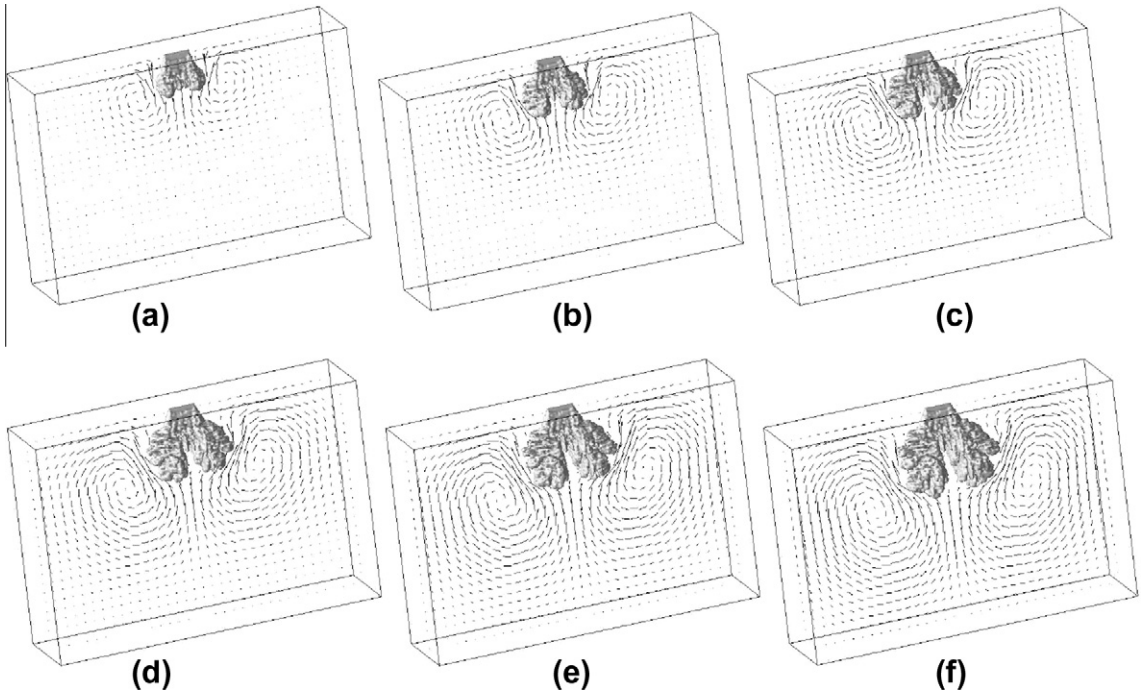

Fig. 15. ECD in a vertical cell: simulation near the spike (enlarged): velocity field superimposed with an anion concentration surface very close to the growth at six successive times.

Acronyms
ECD Electrochemical Deposition
DBM Dielectrical Break-down Model

Acknowledgments

G.G., F.V.M. and G.M. are investigators of the CONICET, Argentina. E.E.M. has a scholarship from CONICET, Argentina. This work was partially supported by grants from CONICET (PIP 1087/09) and Universidad de Buenos Aires (UBACyT X132/08).

References

[1] T. Vicsek, Fractal Growth Phenomena, second ed., World Scientific, Singapore, 1992.
[2] F. Argoul, J. Huth, P. Merzeau, A. Arneodo, H.L. Swinney, Physica D 62 (1993) 170–185, doi:10.1016/0167-2789(93)90279-A.
[3] R.M. Brady, R.C. Ball, Nature 309 (1984) 225–229.
[4] V. Fleury, M. Rosso, J.-N. Chazalviel, B. Sapoval, Phys. Rev. A 44 (10) (1991) 6693–6705, doi:10.1103/PhysRevA.44.6693.
[5] V. Fleury, J.-N. Chazalviel, M. Rosso, Phys. Rev. Lett. 68 (16) (1992) 2492–2495, doi:10.1103/PhysRevLett.68.2492.
[6] V. Fleury, J.-N. Chazalviel, M. Rosso, Phys. Rev. E 48 (2) (1993) 1279–1295, doi:10.1103/PhysRevE.48.1279.
[7] V. Fleury, J. Kaufman, B. Hibbert, Nature 367 (1994) 435–438, doi:10.1038/367435a0.
[8] K.A. Linehan, J.R. de Bruyn, Can. J. Phys. 73 (3–4) (1995) 177–186.
[9] V. Fleury, M. Rosso, J. Chazalviel, in: F. Family, P. Meakin, B. Sapoval, R. Wool (Eds.), Fractal Aspects of Materials, MRS Symp. Proc. Series, Material Research Society, Symp. held November 28–December 1, 1994, Boston, MA, USA, vol. 367, 1995, pp. 183–194.
[10] V. Fleury, M. Rosso, J.-N. Chazalviel, in: H.D. Merchant (Ed.), Symp. on Structure and Properties of Deposits, 3M (Metals Minerals and Materials Society), TMS Publications, Warrendale, Penn, 1995, pp. 195–217.
[11] V. Fleury, J.-N. Chazalviel, in: F. Family, P. Meakin, B. Sapoval, R. Wool (Eds.), Fractal Aspects of Materials, MRS Symp. Proc. Series, Material Research Society, Symp. held November 28–December 1, 1994, Boston, MA, USA, vol. 367, 1995, pp. 169–176.
[12] J. Huth, H. Swinney, W. McCormick, A. Kuhn, F. Argoul, Phys. Rev. E 51 (4) (1995) 3444–3458, doi:10.1103/PhysRevE.51.3444.
[13] J.R. de Bruyn, Phys. Rev. Lett. 74 (1995) 4843–4846.
[14] D.P. Barkey, D. Watt, Z. Liu, S. Raber, J. Electrochem. Soc. 141 (5) (1994) 1206–1212, doi:10.1149/1.2054897.
[15] C. Léger, J. Elezgaray, F. Argoul, Phys. Rev. Lett. 78 (26) (1997) 5010–5013, doi:10.1103/PhysRevLett.78.5010.
[16] J.-N. Chazalviel, Phys. Rev. A 42 (12) (1990) 7355–7367, doi:10.1103/PhysRevA.42.7355.
[17] G. Marshall, E. Perone, P. Tarela, P. Mocskos, Chaos Sol. Fract. 6 (1995) 315–324, doi:10.1016/0960-0779(95)80037-H.
[18] G. Marshall, P. Mocskos, Phys. Rev. E 55 (1) (1997) 549–563, doi:10.1103/PhysRevE.55.549.
[19] G. Marshall, P. Mocskos, H.L. Swinney, J.M. Huth, Phys. Rev. E 59 (2) (1999) 2157–2167, doi:10.1103/PhysRevE.59.2157.
[20] S. Dengra, G. Marshall, F. Molina, J. Phys. Soc. Jpn. 69 (3) (2000) 963–971.
[21] G. González, G. Marshall, F.V. Molina, S. Dengra, M. Rosso, J. Electrochem. Soc. 148 (7) (2001) C479–C487.
[22] G. González, G. Marshall, F. Molina, S. Dengra, Phys. Rev. E 65 (5) (2002) 051607, doi:10.1103/PhysRevE.65.051607. <http://link.aps.org/abstract/PRE/v65/e051607>.
[23] G. Marshall, E. Mocskos, F.V. Molina, S. Dengra, Phys. Rev. E 68 (2) (2003) 021607, doi:10.1103/PhysRevE.68.021607.
[24] S. Dengra, Experimental and Theoretical Studies of Ion Transport in Thin-layer Electrodeposition Cells, PhD Thesis, Departamento de Computación, Universidad de Buenos Aires, August 2004 (in Spanish).
[25] G. Marshall, F. Molina, A. Soba, Electrochim. Acta 50 (16–17) (2005) 3436–3445, doi:10.1016/j.electacta.2004.12.018. <http://www.sciencedirect.com/science/article/B6TG0-4F9F833-2/2/fe6e39dfd5fbde3a9b0646640800942a>.
[26] E. Mocskos, G. Marshall, Electron. Trans. Numer. Anal. 34 (2009) 90–101.
[27] M. Rosso, J.-N. Chazalviel, V. Fleury, E. Chassaing, Electrochim. Acta 39 (4) (1994) 507–515.
[28] J.N. Chazalviel, M. Rosso, E. Chassaing, V. Fleury, J. Electroanal. Chem. 407 (1–2) (1996) 61–73. <http://www.sciencedirect.com/science/article/B6TGB-3V9C8H2-7/2/9ef6f8735767a12ad961d70390cc21a8>.
[29] M. López-Salvans, P. Trigueros, S. Vallmitjana, J. Claret, F. Sagués, Phys. Rev. Lett. 76 (21) (1996) 4062–4065, doi:10.1103/PhysRevLett.76.4062.
[30] Y. Fukunaka, K. Okano, Y. Tomii, Z. Asaki, K. Kuribayashi, J. Electrochem. Soc. 145 (6) (1998) 1876–1881, doi:10.1149/1.1838570. <http://link.aip.org/link/?JES/145/1876/1>.
[31] G. Marshall, E. Mocskos, G. González, S. Dengra, F.V. Molina, C. Iemmi, Electrochim. Acta 51 (15) (2006) 3058–3065.
[32] M. Abramoff, P. Magelhaes, S. Ram, Biophoton. Int. 11 (7) (2004) 36–42.
[33] A.J. Bard, L.R. Faulkner, Electrochemical Methods, Fundamentals and Applications, John Wiley & Sons, New York, 1980.
[34] J. Newman, K. Thomas-Alyea, Electrochemical Systems, third ed., John Wiley & Sons, Inc., Hoboken, NJ, 2004.

[35] R.F. Probstein, Physicochemical Hydrodynamics, An Introduction, second ed., John Wiley & Sons, New York, 1994.
[36] V. Levich, Physicochemical Hydrodynamics, Prentice Hall, New Jersey, 1962.
[37] G.D. Mallinson, G. de Vahl Davis, J. Comput. Phys. 12 (4) (1973) 435–461. doi:10.1016/0021-9991, <http://www.sciencedirect.com/science/article/B6WHY-4DDR59S-YY/2/6521aa56919362d3dae676c4c758f31e>.
[38] G.D. Mallinson, G. de Vahl Davis, J. Fluid Mech. 83 (1) (1977) 1–31, doi:10.1017/S0022112077001013.
[39] L. Pietronero, H.J. Weismann, J. Stat. Phys. 36 (5) (1984) 909–916, doi:10.1007/BF01012949. <www.springerlink.com/content/jn25p7462l806675>.
[40] Opendx: An Open Source Imaging Package, <http://www.opendx.org>.